

# Exploring Charged Higgs at the Future Circular Collider (FCC): A Review of Two-Higgs-Doublet Models

Ijaz Ahmed,<sup>1,\*</sup> Basit Ali,<sup>1,†</sup> M.S. Amjad,<sup>2,‡</sup> M. Jamil,<sup>3,§</sup> Saba Shafaq,<sup>4,¶</sup> and Usman Ahmad<sup>5,\*\*</sup>

<sup>1</sup>*Physics Department, Federal Urdu University of Arts,*

*Science and Technology Islamabad, Pakistan*

<sup>2</sup>*National University of Technology, Islamabad*

<sup>3</sup>*Department of Physics, Konkuk University, Seoul South Korea*

<sup>4</sup>*International Islamic University Islamabad Pakistan*

<sup>5</sup>*Riphah International University, Islamabad Pakistan*

(Dated: November 8, 2024)

## Abstract

In this paper, we report the theoretical investigation on the charged Higgs bosons and their coupling to fermions within the Two Higgs Doublet Model (THDM). The study is focused on the discovery potential of the charged Higgs bosons as predicted in the Type-III and IV at the future circular hadron-hadron collider (FCC-hh) at  $\sqrt{s} = 100$  TeV. Using their decays, coupling to fermions, branching ratios, and production cross section via  $pp \rightarrow tH^-$ , we investigated for the signatures of charged Higgs bosons, along with the kinematical distributions based on the background processes of  $b\bar{b}$  quarks. We exploited two reference points and experimental constraints to determine an upper bound on the mass of charged Higgs in the 200–1000 GeV range. We found that  $H^- \rightarrow b\bar{t}$  and  $H^- \rightarrow W^- A$  become high priorities in probing additional charged Higgs channels. We also presented the application of modern machine learning techniques such as Boosted Decision Tree (BDT), likelihood (LH), and Multilayer Perceptron (MLP) as an alternate approach to light-charged Higgs boson production in association with W boson in THDM Type-I via weak interaction, demonstrating its observability against the most relevant electroweak Standard Model backgrounds.

PACS numbers: 12.60.Fr, 14.80.Fd

Keywords: Charged Higgs, MSSM, LHC

---

\*Electronic address: Ijaz.ahmed@fuuast.edu.pk

†Electronic address: basit4319@gmail.com

‡Electronic address: sohailamjad@nutech.edu.pk

§Electronic address: mjamil@konkuk.ac.kr

¶Electronic address: saba.shafaq@iiu.edu.pk

\*\*Electronic address: usmanahmed1661@gmail.com

## I. INTRODUCTION

The standard model (SM) of particle physics has provided a remarkably successful electroweak theory, which is consistent with the current experimental observations. This was particularly recognized by the milestone discovery of the final constituent of the SM, the neutral spin-zero Higgs boson at the LHC in 2012 with a mass of about 125 GeV [1, 2]. Besides solving many longstanding fundamental problems of modern physics in light of the predictions of the SM, such as unitarity of high energy scattering amplitude involving massive weak gauge bosons ( $W^\pm$  and  $Z$ ) and renormalization of the electroweak theory [3], the Brout-Englert-Higgs (BEH) process was finally validated by the discovery of the Higgs boson scalar in [4].

In the SM, the BEH mechanism not only explains the origin of mass for the gauge bosons ( $W^\pm$  and  $Z$ ) and charged fermions (quarks and leptons) via spontaneous electroweak symmetry breaking (EWSB), but it also ensures unitarity of high energy amplitude. The masses of the SM particles emerge from their coupling to the Higgs boson. This further established the fact that mass is not an intrinsic property of particles. However, particles (like photons) have zero mass because they don't interact with the Higgs field. The Higgs boson is an excitation of the Higgs field having non-zero vacuum expectation value (vev). After the discovery of Higgs boson, measuring its coupling to the SM particles via EWSB is the next priority. Experimental sensitivity to the Higgs coupling comes from measurements of the Higgs production cross sections, decay modes, branching fractions, and total decay width. For further validation of the Higgs coupling to the particles having mass via EWSB it was imperative to extend the Higgs sector to BSMs in search for the discovery potential of new particles and Higgs bosons coupled with the Higgs boson of the SM and BSMs. Further, despite the marvelous success of the SM, some theoretical as well as experimental evidence suggest that the SM is only a low-scale effective theory of a more fundamental one at high energy, hence such evidence calls for the extension of the SM too.

The extension is also necessary to solve some existing puzzles in the SM such as an abundance of dark matter that is about 80 % of the total matter contents of the Universe, dark energy that renders accelerating expansion of the Universe, matter-antimatter asymmetry rendering abundance of baryonic matter, the hierarchy problem that deals with the huge mismatch between EW scale and the Planck scale, neutrino mass problem via neutrino oscillations, and quantization of gravity, etc. The evidence of the extended Higgs sector and departure from the SM will be marked by a new discovery of single or several extra Higgs bosons. In theories with two Higgs doublets, the existence of charged Higgs bosons  $H^\pm$  is an integral component. Also, charged scalars are commonly

predicted in models where we add one extra scalar doublet  $SU(2)_L$  in the SM Higgs sector. Hence, if they are discovered, it will be clear evidence for BSM physics.

## II. TWO HIGGS DOUBLET MODEL AND BENCHMARKING

The Two Higgs Doublet Model (2HDM) is a very simple approach to test the signatures of the extended Higgs sector. There are four types of 2HDMs. All quarks and leptons couple to the  $\Phi_2$  scalar field in Type-I. In Type-II, down quarks and charged leptons acquire their masses from the  $\Phi_1$  scalar field, whereas up quarks gain their mass from the  $\Phi_2$  coupling. All charged leptons couple to  $\Phi_1$  in Type-X (or Type-III), whereas all quarks couple to  $\Phi_2$ . Hence, Type III is also called lepton specific model. In Type-Y (or Type-IV), all down quarks gain their masses from  $\Phi_1$  while up quarks and charged leptons acquire their masses from  $\Phi_2$ . The 2HDMs models predict a total of five Higgs bosons, which include two  $CP$ -even,  $h$  (lighter Higgs),  $H$  (heavy Higgs), one  $CP$ -odd  $A$  (pseudoscalar Higgs) and two more charged Higgs bosons  $H^\pm$ . In 2HDMs, there are two scalar doublets having scalar fields  $\Phi_1$  &  $\Phi_2$  and hyper-charge  $Y = \frac{1}{2}$ . For the detailed theory and phenomenology of 2HDMs models, the interested readers are referred to [5]. As of now, 2HDM of Type-I and Type-II have attracted greater attention [4, 5, 7],[8–10], in particular with regard to the searches of extended Higgs sector at the future circular hadron-hadron collider (FCC-hh). 2HDM Type-III has been also invoked by some researchers [11–14] to investigate the signatures of Higgs bosons beyond the SM. However, there is lack of studies on 2HDM Type-III and Type-IV regarding the discovery potential of the charged Higgs bosons via channel  $pp \rightarrow tH^-$ , with the kinematical distributions in the background processes of  $b\bar{b}$  quarks at the future circular hadron-hadron collider (FCC-hh) at center of mass energy  $\sqrt{s} = 100$  TeV. In particular, the current study is aimed at searching for the signatures of the charged Higgs bosons through their decays, coupling to fermions, branching ratios and production cross-section. We employed the two required benchmark points together with experimental constraints to determine an upper bound on the mass of charged Higgs in the 200-1000 GeV range. The same channel has been investigated in [5], using 2HDMs of Type-I and Type-II with similar constraints. The two benchmark points for the channels under investigation are  $M_H^\pm = M_H$  &  $M_A = 100$  GeV as BP1 and  $M_H^\pm = M_H = M_A$  as BP2. The preferred condition for experimentalists is the alignment limit  $\sin(\alpha - \beta) \rightarrow 1$ . For this limit, neutral scalar Higgs  $h$  behaves like SM Higgs having a mass 125 GeV. For this condition, the heavy Higgs  $H$  in 2HDM is gauge phobic because couplings to  $W/Z$  are suppressed. In this alignment limit the decay  $H^\pm \rightarrow W^\pm h$  vanishes completely. A limit on charged Higgs mass and  $\tan\beta$  plane has already been

set from LHC experiments at  $\sqrt{s}=8$  TeV for  $H^\pm \rightarrow \tau^\pm\nu$  [17, 18] &  $H^+ \rightarrow t\bar{b}$  [19, 20] decay modes. For  $M_H^\pm = 80 - 160$  GeV, the significant constraint arises from the decay channel  $H^\pm \rightarrow t\bar{b}$ . The scheme to probe charged Higgs  $H^\pm$  has mass dependence that tells us about the total cross-section and also decay available channels, which can be grouped in two types; low and high mass cross-section scenarios. For low mass of charged Higgs, if it satisfies the condition  $m_t > m_H^\pm$  then the decay of charged Higgs  $H^\pm$  to  $\tau\nu$  channel becomes dominant in the region where  $\tan\beta > 1$  and  $H^+$  can be produced via the  $t \rightarrow H^+\bar{b}$  decay channel. However for  $\tan\beta > 1$  decay  $t \rightarrow W^+b$  becomes dominant for both 2HDM-I and 2HDM-II. Here we have imposed the condition that  $m_{H^\pm} = M_{W^\pm}$ . For the production cross-section, we have considered the process  $pp \rightarrow tH^+$  calculated at FCC-hh Collider. We have found that for large masses the decay mode  $H^+ \rightarrow t\bar{b}$  is dominant. Our results show that  $pp \rightarrow \bar{t}H^+$  is the dominant channel for charged Higgs production given by  $g\bar{b} \rightarrow H^+\bar{t}$ . From Figure 1 The relation between production cross section  $\sigma$  and charged Higgs mass  $M_{H^\pm}$  at different future hadron colliders figure.captio.3, we can see a comparison of cross sections of charged Higgs production at different particle colliders. The charged Higgs boson production cross section in the 2HDM type III model varies significantly with the value of  $\tan\beta$ , with enhanced production at high values of  $\tan\beta$  due to the increased mixing between the two Higgs doublets. The production cross-section also depends on the mass of the charged Higgs boson and the specific production channel. Type IV 2HDMs, exhibit a non-monotonic behavior with  $\tan\beta$ , with a minimum at intermediate values of  $\tan\beta$  due to top quark decays. The exact value of this minimum depends on the specific parameters of the model.

### III. BACKGROUND PHENOMENOLOGY

The Lagrangian  $\mathcal{L}$  of 2HDM is given as;

$$\mathcal{L}_S = \sum_{i=1}^2 (\mathcal{D}_\mu \Phi_i)^\dagger (\mathcal{D}^\mu \Phi_i) - V_{THDM} \quad (1)$$

And covariant derivative is represented as,

$$\mathcal{D}_\mu = \partial_\mu - \frac{i}{2}g \sum_{\alpha=1}^3 \sigma^\alpha \mathcal{W}_\mu^\alpha - \frac{i}{2}g' \mathcal{B}_\mu \quad (2)$$

The general Higgs potential is given as;

$$\begin{aligned} V_{THDM} = & m_1^2 |\phi_1^2| + m_2^2 |\phi_2^2| - m_3^2 |\phi_1^\dagger \phi_2| + h.c. \\ & + \frac{1}{2} \lambda_1 |\phi_1^4| + \frac{1}{2} \lambda_2 |\phi_2^4| + \lambda_3 |\phi_1^2| |\phi_2^2| + \lambda_4 |\phi_1^\dagger \phi_2|^2 \\ & + \frac{1}{2} \lambda_5 (\phi_1^\dagger \phi_2)^2 + \lambda_6 |\phi_1|^2 \phi_1^\dagger \phi_2 + \lambda_7 |\phi_2|^2 \phi_1^\dagger \phi_2 + h.c. \end{aligned} \quad (3)$$

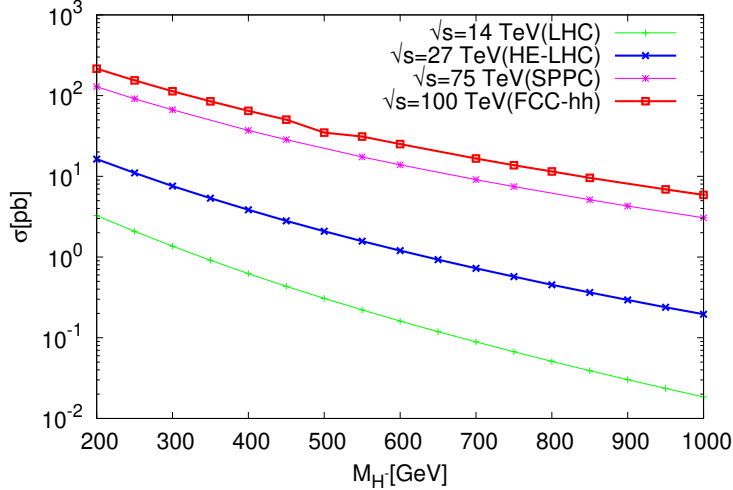


FIG. 1: The relation between production cross section  $\sigma$  and charged Higgs mass  $M_{H^\pm}$  at different future hadron colliders

Here  $m_1$ ,  $m_2$  and  $\lambda_1$ - $\lambda_4$  are real parameters and  $m_3$  &  $\lambda_5$ - $\lambda_7$  are complex in nature. Both Higgs doublets are given by;

$$\phi_1 = \begin{pmatrix} \omega_1^+ \\ \frac{1}{\sqrt{2}}(\nu_1 + h_1 + iz_1) \end{pmatrix} \quad (4)$$

$$\phi_2 = \begin{pmatrix} \omega_2^+ \\ \frac{1}{\sqrt{2}}(\nu_2 + h_2 + iz_2) \end{pmatrix} \quad (5)$$

In 2HDM, the charged Higgs boson can decay into a pair of fermions through Yukawa interactions. The partial decay width of this process depends specifically on the nature of the coupling between the charged Higgs boson and the fermions. In the type III 2HDM, the charged Higgs boson couples to the down-type quarks and leptons, while the up-type quarks do not couple directly. The partial decay width for the charged Higgs boson decaying into a down-type quark and an anti-down-type quark is given by:

$$\Gamma(H^\pm \rightarrow q_d \bar{q}_d) = \frac{m_{H^\pm}^3}{16\pi} \left[ \frac{m_q}{v_2} \right]^2 \left[ \frac{1}{2} - \frac{m_q^2}{m_{H^\pm}^2} \right]^2 \quad (6)$$

where  $m_q$  is the mass of the down-type quark,  $m_{H^\pm}$  is the mass of the charged Higgs boson,  $v_2$  is the vacuum expectation value of the second Higgs doublet, and the factor of 1/2 in the square brackets is the D-term factor that arises due to the non-diagonal nature of the quark mass matrix in the type III 2HDM. In the type IV 2HDM, the charged Higgs boson couples to both up-type and

down-type quarks and leptons, but the coupling strengths are different for each type of fermion. The partial decay width for the charged Higgs boson decaying into a down-type quark and an anti-down-type quark (c or s) is given by:

$$\Gamma(H^\pm \rightarrow q_d \bar{q}_d) = \frac{m_{H^\pm}^3}{16\pi} \left[ \frac{m_q}{v_2} \sin(\beta - \alpha) + \frac{m_q}{v_1} \cos(\beta - \alpha) \right]^2 \left[ \frac{1}{2} - \frac{m_q^2}{m_{H^\pm}^2} \right]^2 \quad (7)$$

where  $v_1$  and  $v_2$  are the vacuum expectation values of the two Higgs doublets, and  $\alpha$  is the mixing angle between the two doublets. The factor of  $\sin(\beta - \alpha)$  and  $\cos(\beta - \alpha)$  in the square brackets arises due to the different coupling strengths between the charged Higgs boson and the down-type quarks in the type IV 2HDM. In both cases, the partial decay width is proportional to the cubic power of the charged Higgs boson mass and the square of the fermion mass, and it decreases rapidly as the invariant mass of the fermion pair approaches the mass of the charged Higgs boson.

#### IV. CHARGED HIGGS COUPLINGS

In 2HDM, there are two Higgs doublets, and the charged Higgs boson arises as a result of the mixing between the two doublets. The strength of the interaction between the charged Higgs boson and other particles is determined by the charged Higgs coupling constants. In the Type III and Type IV variants of the 2HDM, the charged Higgs coupling constants are given by the following formulas in terms of the masses of the particles involved.

##### A. Type III

The charged Higgs boson ( $H^\pm$ ) couples differently to quarks, leptons, and gauge bosons compared to the Standard Model (SM). Here are the charge Higgs coupling relations in 2HDM type III: The charged Higgs coupling relations in 2HDM type III can be expressed as follows:

##### 1. Up-type quarks

The coupling strength between the charged Higgs boson and an up-type quark ( $u$ ) is given by:

$$g_{uH^\pm} = -\frac{m_u}{\sqrt{2}v_2} \sin(\beta - \alpha) \quad (8)$$

where  $v_2$  is the vacuum expectation value (VEV) of the second Higgs doublet,  $\beta$  is the mixing angle between the two Higgs doublets, and  $\alpha$  is a second mixing angle that appears in 2HDM type III.

2. *Down-type quarks*

The coupling strength between the charged Higgs boson and a down-type quark ( $d$ ) is given by:

$$g_{dH^\pm} = -\frac{m_d}{\sqrt{2}v_1} \cos(\beta - \alpha) \quad (9)$$

where  $v_1$  is the VEV of the first Higgs doublet.

3. *Leptons*

The charged Higgs boson couples to leptons through their Yukawa couplings with the first Higgs doublet, and the coupling strength is given by:

$$g_{lH^\pm} = -\frac{m_l}{\sqrt{2}v_1} \quad (10)$$

4. *Gauge bosons*

The charged Higgs boson couples to gauge bosons through their mixing with the W boson, which depends on the mass of the charged Higgs boson and the mixing angle  $\beta$ . The coupling strength is given by:

$$g_{W^\pm H^\pm} = -\frac{g}{\sqrt{2}}(1 + \tan^2 \beta) + \frac{gm_{W^\pm}}{m_{H^\pm}^2}(1 + \tan^2 \beta) \sin(2\beta) \quad (11)$$

where  $g$  is the SU(2) gauge coupling constant.

**B. Type IV**

The charged Higgs couplings to quarks and leptons are given by: In this model, the charged Higgs boson couples to up-type quarks ( $u$  and  $c$ ) and their corresponding charged leptons ( $e$  and  $\mu$ ) through Yukawa couplings. The strength of these couplings is given by:

1. *Up-type quarks*

Light quarks ( $u$  and  $c$ ):

$$g_{H^\pm u\bar{d}} = -g_{H^\pm c\bar{s}} = \frac{m_u}{v_1} \sin(\beta - \alpha) + \frac{m_c}{v_2} \cos(\beta - \alpha) \quad (12)$$

Heavy quarks ( $t$ ):

$$g_{H^\pm t \bar{b}} = -\frac{m_t}{v_2} \cos(\beta - \alpha) \quad (13)$$

where  $v_1$  and  $v_2$  are the vacuum expectation values (VEVs) of the two Higgs doublets,  $\beta$  is the mixing angle between the two doublets, and  $\alpha$  is a second mixing angle that appears in this model. The first term in each coupling represents the contribution from the type I Yukawa sector, while the second term represents the contribution from the type II Yukawa sector.

### 2. Charged leptons

Light leptons ( $e$  and  $\mu$ ):

$$g_{H^\pm e \bar{\nu}_e} = -g_{H^\pm \mu \bar{\nu}_\mu} = \frac{m_e}{v_1} \sin(\beta - \alpha) + \frac{m_\mu}{v_2} \cos(\beta - \alpha) \quad (14)$$

Heavy leptons ( $\tau$ ):

$$g_{H^\pm \tau \bar{\nu}_\tau} = -\frac{m_\tau}{v_2} \cos(\beta - \alpha) \quad (15)$$

### 3. Gauge bosons

The charged Higgs boson also interacts with gauge bosons (W and Z) through gauge interactions. The coupling strengths are given by:

$$g_{H^\pm W^\mp} = -\frac{g}{\cos \theta_W} (\sin(\beta - \alpha) - \cos(\beta - \alpha)) \quad (16)$$

$$g_{H^\pm Z} = -\frac{g}{\cos \theta_W} (\sin(\beta - \alpha) \cos^2 \theta_W + \cos(\beta - \alpha) \sin^2 \theta_W) \quad (17)$$

where  $g$  is the weak coupling constant and  $\theta_W$  is the weak mixing angle. These couplings depend on both mixing angles  $\alpha$  and  $\beta$ .

## V. RESULTS AND DISCUSSIONS

By inserting all the interaction vertices relations in CalcHEP, we have calculated the decay width and branching fractions and also production cross-section for both benchmark points BP-I and BP-II. Here the alignment limit  $\sin(\beta - \alpha)$  is considered to have the value 1. So, in this case, lighter Higgs having mass 125 GeV behaves like SM Higgs.



All the results are presented from Figure 2. Plot is shown between  $M_{H^\pm}$  and  $\%Sigma$  for  $\tan\beta = 1$ . Here, the Plot (a) shows the decay width of charged Higgs to all possible decay modes for BP-I. While Plot (b) shows BR of charged Higgs to all possible decay modes for BP-II. Figure 16 - Figure 16 The MLP cut efficiencies as a function of applied cut values. figure.captio.40 which include total decay width, branching ratios, and kinematical distributions of the bottom (anti-bottom) quarks from background processes.

### A. Total Decay Width of Charged Higgs

The total decay width of charged Higgs for both parameters BP-I and BP-II is shown in Figure 2. Plot is shown between  $M_{H^\pm}$  and  $\%Sigma$  for  $\tan\beta = 1$ . Here, the Plot (a) shows the decay width of charged Higgs to all possible decay modes for BP-I. While Plot (b) shows BR of charged Higgs to all possible decay modes for BP-II. Figure 3. Plot between  $M_{H^\pm}$  and BR in  $\%$  for  $\tan\beta = 1$ . Plot (a) shows the BR of charged Higgs to all possible decay modes for BP-I. Plot (b) shows BR of charged Higgs to all possible decay modes for BP-II. Figure 19 for both models THDM type-III and type-IV. From the figures shown below for total decay width one can see that whenever the mass of charged Higgs increases from 300 GeV, the change in decay width is very small, and for large  $\tan\beta$  values it remains almost constant. For  $\tan\beta=7$ , the decay width is minimum e.g using both BP-I and BP-II for THDM-II, and for the mass of charged Higgs  $m_{H^-} = 300$  GeV, the value obtained for decay width is given as  $\Gamma = 5 \times 10^0 (3.5 \times 10^{-1})$  GeV, which is illustrated in Figure 2. Plot is shown between  $M_{H^\pm}$  and  $\%Sigma$  for  $\tan\beta = 1$ . Here, the Plot (a) shows the decay width of charged Higgs to all possible decay modes for BP-I. While Plot (b) shows BR of charged Higgs to all possible decay modes for BP-II. Figure 17.

### B. Charged Higgs Branching Ratios of THDM-III

For BP-I the plot between the mass of charged Higgs and branching fractions is shown in Figure 3. Plot between  $M_{H^\pm}$  and BR in  $\%$  for  $\tan\beta = 1$ . Plot (a) shows the BR of charged Higgs to all possible decay modes for BP-I. Plot (b) shows BR of charged Higgs to all possible decay modes for BP-II. Figure 19. To understand these decay channels of charged Higgs in more detail, graphical analysis is always there, by putting all data in Gnuplot, the graph is plotted between  $M_{H^\pm}$  and BR which is shown in Figure 3(b). It is obvious decay that  $H^- \rightarrow b\bar{t}$  is highly dominant which is almost 100%.

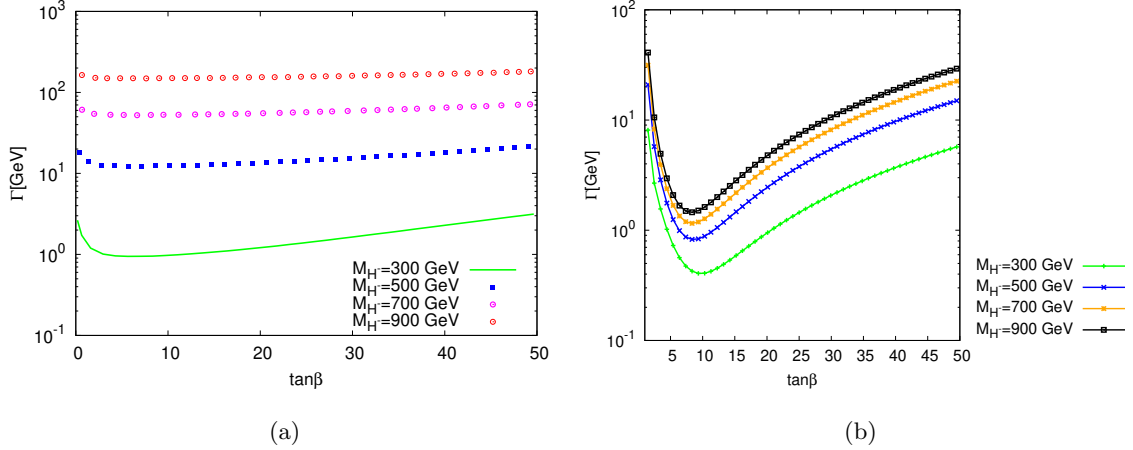


FIG. 2: Plot is shown between  $M_{H^\pm}$  and  $\%Sigma$  for  $\tan\beta = 1$ . Here, the Plot (a) shows the decay width of charged Higgs to all possible decay modes for BP-I. While Plot (b) shows BR of charged Higgs to all possible decay modes for BP-II

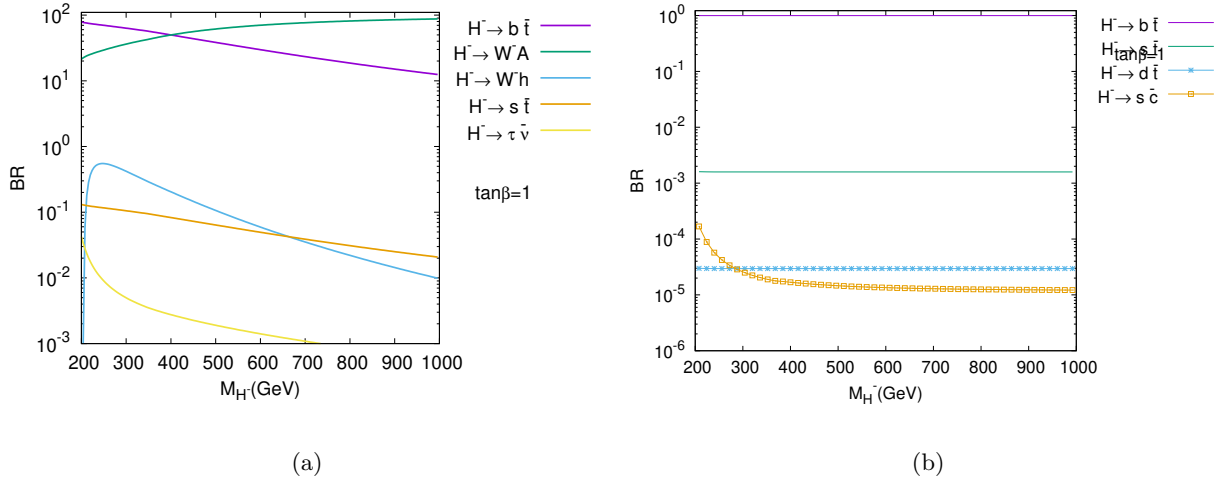


FIG. 3: Plot between  $M_{H^\pm}$  and BR in % for  $\tan\beta = 1$ . Plot (a) shows the BR of charged Higgs to all possible decay modes for BP-I. Plot (b) shows BR of charged Higgs to all possible decay modes for BP-II

### C. Charged Higgs Branching Ratios of THDM-IV

In the case of THDM-IV, the same thing happens as in the case of THDM-III. Here the dominant decay mode is also  $H^- \rightarrow W^- A$  channel. Because for the condition where  $M_{A^0} < M_t$  it opens a bosonic channel. Hence decay to this channel becomes dominant. To illustrate this graphically, the values are plotted between  $M_{H^\pm}$  and BR which is shown in Figure 4

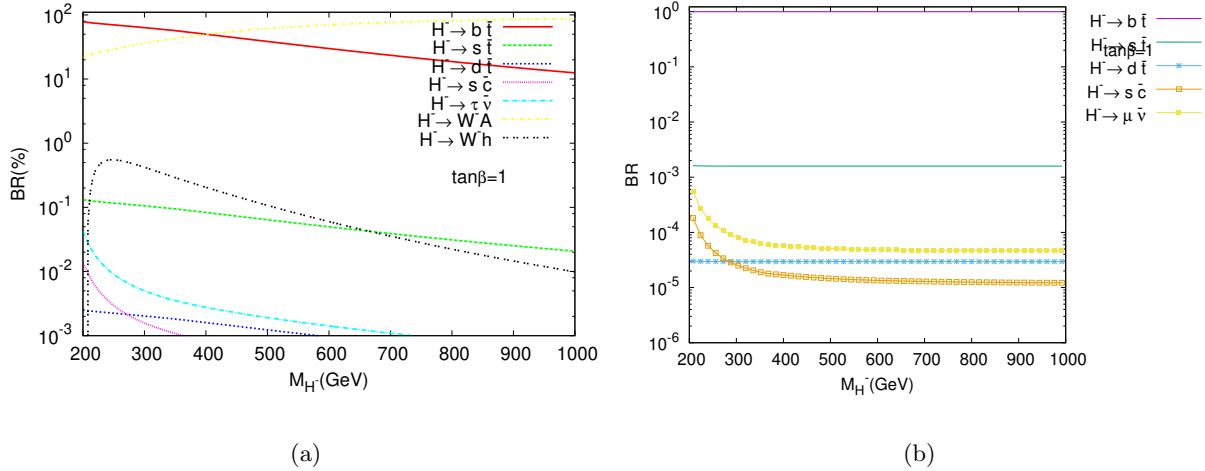


FIG. 4: Plot between  $M_{H^\pm}$  and %BR for  $\tan\beta=1$ . Fig. (a) shows BR of charged Higgs for all possible decay modes for BP-II. Fig. (b) shows BR of charged Higgs to all possible decay modes for BP-I

%BR for  $\tan\beta=1$ . Fig. (a) shows BR of charged Higgs for all possible decay modes for BP-II. Fig. (b) shows BR of charged Higgs to all possible decay modes for BP-I. Here we can see that dominant decay is again  $b\bar{t}$  channel and has BR up to 91%. The BR to other decay channels is almost constant, which shows the independence of BR from  $\tan\beta$ . The  $b\bar{t}$  is dominant because top quarks have the largest mass of all fermions. Hence for Higgs mass greater than top quarks masses the decay channel  $b\bar{t}$  becomes dominant. All rest decay modes are lowered or we can say that they are suppressed.

## VI. COMPARATIVE RESULTS

In this section, a comparative view of the plots is presented of all THDMs. Figure 5 Total Decay width of charged Higgs as a function of  $\tan\beta$  for  $M_H^\pm = 500$  GeV of all THDMs and Figure 6(a) The total Decay width of charged Higgs as a function of  $M_H^\pm$  for  $\tan\beta = 7$  of all THDMs. (b) Plot between %BR and  $M_H^\pm$  for the decay  $H^- \rightarrow b\bar{t}$  of all THDMs show the plots for the total decay width of charged Higgs depending on  $\tan\beta$  for  $M_H^\pm = 500$  GeV. It can be seen that the decay width for Type-III and Type-IV have the same values as expected from couplings. Because for both type-III and type-IV the quarks couples to the same type of scalar field. The decay width for type-IV has a little bit of less value this is because leptons couples to another type of scalar field which is inverse of  $\tan\beta$  i.e  $\cot\beta$ .

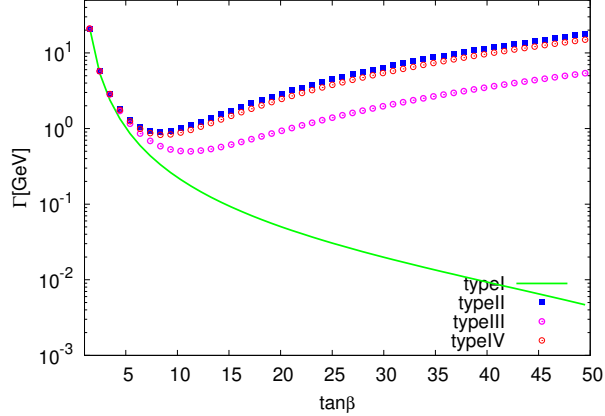


FIG. 5: Total Decay width of charged Higgs as a function of  $\tan \beta$  for  $M_H^\pm = 500$  GeV of all THDMs

For type-I and type-III, the situation is very different because in the case of type-I all fermions couple to the same type of scalar field so the decay width decreases with the increasing values of  $\tan \beta$ . In the case of type-III, the decay width is less than type-II and IV, but it increases due to leptons couplings with the same type of scalar field. In **Figure 6(a) The total Decay width of charged Higgs as a function of  $M_H^\pm$  for  $\tan \beta = 7$  of all THDMs.** (b) **Plot between %BR and  $M_H^\pm$  for the decay  $H^- \rightarrow b\bar{t}$  of all THDMs**figure.captio.24, The total decay width of charged Higgs as a function of the mass of charged Higgs for  $\tan \beta = 7$  of all THDMs are shown. We can see that the decay width for THDM type-I is minimal as expected from coupling relations. Again in the case of type-III the decay width is a little less than type-II and type-IV, but as in the case of type-III the leptons couple to the same type of field so it gives almost the same values as type-III and type-IV. In Figure 7Plot between  $\sigma$  and  $M_{H^\pm}$  at different future colliders for THDM-III (left) and THDM-IV (right)figure.captio.26, a plot between %BR and mass of charged Higgs for the decay  $H^- \rightarrow b\bar{t}$  of all THDMs is presented. It can be seen clearly that it is the dominant decay mode of all THDMs, the graphic line overlap for all THDMs which is clear evidence that the dominant decay mode is  $b\bar{t}$  channel of all THDMs.

## VII. PRODUCTION CROSS SECTIONS

In particle physics, the cross-section is concerned with particle contact. The cross-section of any process is the measure of the likelihood that two particles will interact with each other. In

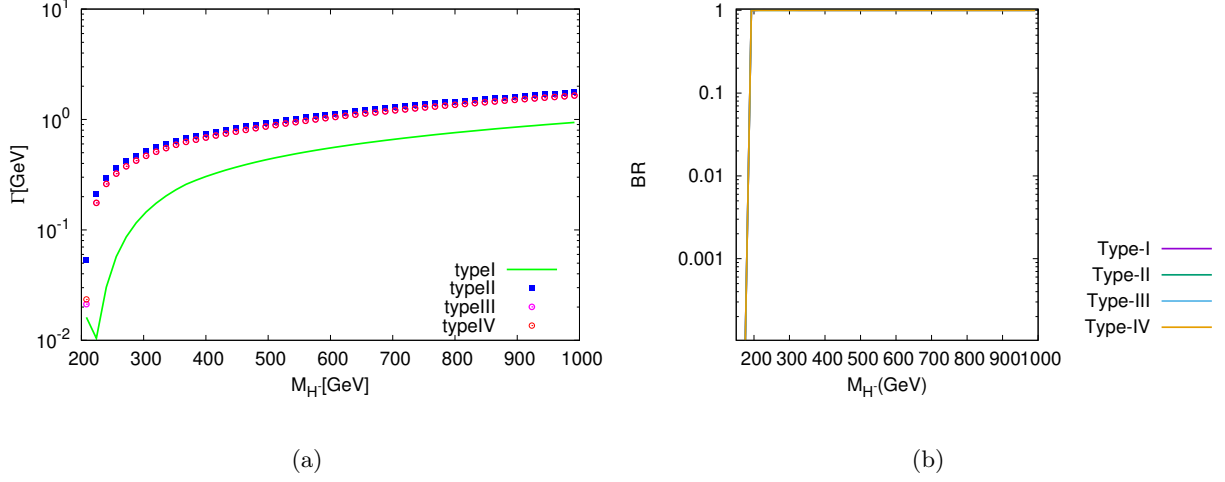


FIG. 6: (a) The total Decay width of charged Higgs as a function of  $M_H^\pm$  for  $\tan\beta = 7$  of all THDMs. (b) Plot between %BR and  $M_H^\pm$  for the decay  $H^- \rightarrow b\bar{t}$  of all THDMs

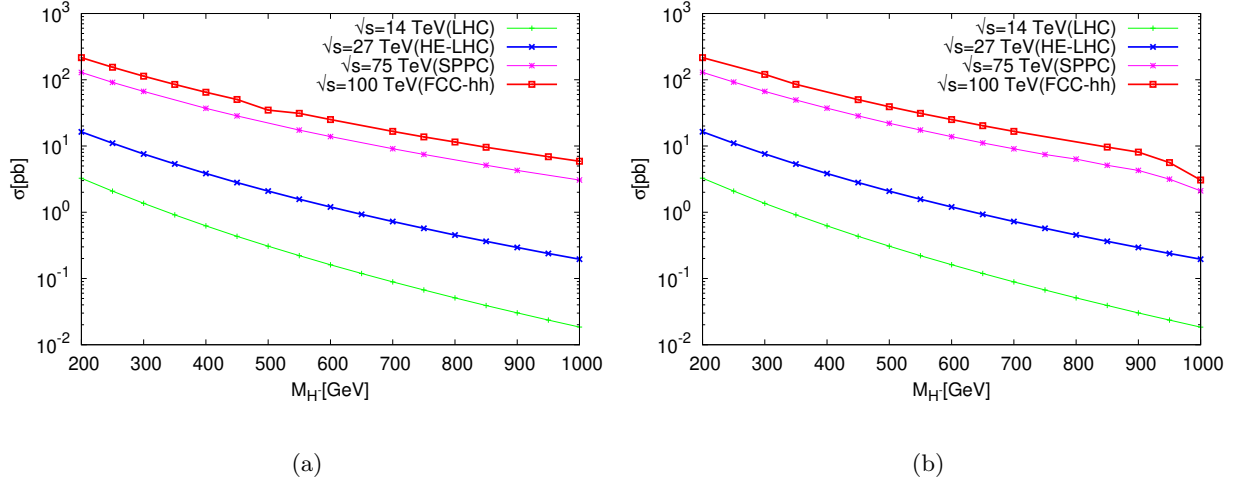


FIG. 7: Plot between  $\sigma$  and  $M_{H^\pm}$  at different future colliders for THDM-III (left) and THDM-IV (right)

a very simple way, the cross-section can be defined as an effective area in which the reaction will take place. From Figure 7 Plot between  $\sigma$  and  $M_{H^\pm}$  at different future colliders for THDM-III (left) and THDM-IV (right) figure.captio.26, we can also see the same situation, the cross-section decreases for large  $\tan\beta$  values. However, its value is maximum for  $\tan\beta = 50$  and  $60$ . It can be seen from coupling relations that increasing  $\tan\beta$  values increases the down quarks coupling values and leptons too. At large  $\tan\beta$  leptons contribute to significant cross-section values, which results in greater cross-section values. Thus, the cross-section has units of area and in nuclear and particle

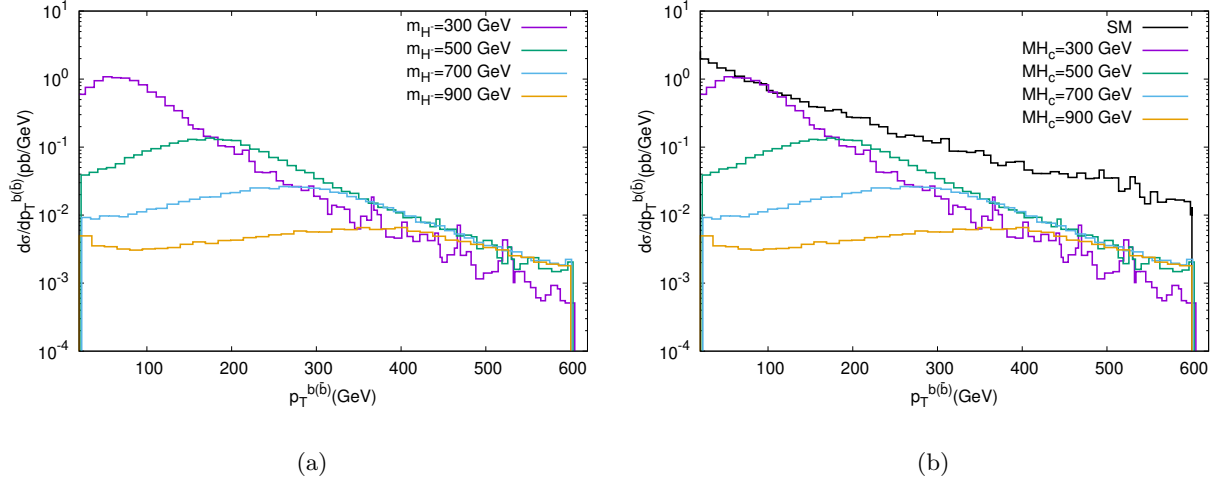


FIG. 8:  $P_T$  distributions of  $b(\bar{b})$  quarks of THDM-III. Fig. (a) shows transverse momentum distributions for BP-I and Fig. (b) shows transverse momentum distributions for BP-II

physics the following definition is used, where  $1 \text{ barn} = 10^{-24} \text{ cm}^2$ . A more detailed explanation can be found in [23].

Here in Figure 6(a) The total Decay width of charged Higgs as a function of  $M_H^\pm$  for  $\tan \beta = 7$  of all THDMs. (b) Plot between %BR and  $M_H^\pm$  for the decay  $H^- \rightarrow b\bar{t}$  of all THDMs figure.caption.24 - Figure 7 Plot between  $\sigma$  and  $M_{H^\pm}$  at different future colliders for THDM-III (left) and THDM-IV (right) figure.caption.26, the plots between production cross section as a function of mass presented for the models THDM type-I, type-II, type-III, and type-IV for the process  $pp \rightarrow tH^+$ , for different colliders i.e LHC ( $\sqrt{s} = 14 \text{ TeV}$ ), HE-LHC ( $\sqrt{s} = 27 \text{ TeV}$ ), SPPC ( $\sqrt{s} = 75 \text{ TeV}$ ) and FCC-hh ( $\sqrt{s} = 100 \text{ TeV}$ ).

From cross-section plots, it can be seen that production cross-section is maximum for FCC-hh as it should be because it has a higher center of mass energy. So it will provide a wide range of parameter space for charged Higgs detection. The same scenario can be given for SPPC as it also provides a larger cross-section.

### VIII. TRANSVERSE MOMENTUM DISTRIBUTIONS

It is necessary to measure the momentum of particles that are produced when particles collide. Now momentum has two components a transverse and longitudinal component. The significant property of the transverse component is that it is invariant under Lorentz transformation. It is denoted by  $p_T$ .

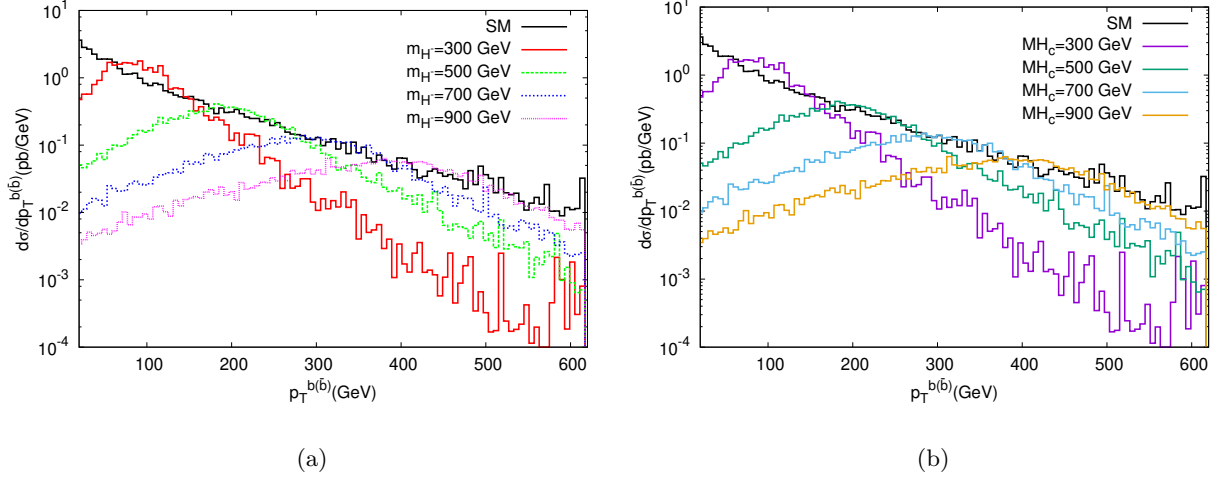


FIG. 9:  $P_T$  distributions of  $b(\bar{b})$  quarks of THDM-IV. Here, the Fig.9(a) shows transverse momentum distributions for BP-I and Fig.9(b) shows transverse momentum distributions for BP-II

The following conventions are adopted to obtain Cartesian momentum  $p_x, p_y$ , and  $p_z$ .

$$p_x = p_T \cos \phi \quad (18)$$

$$p_y = p_T \sin \phi \quad (19)$$

$$p_z = p_T \sinh \eta \quad (20)$$

In order to distinguish the signal and background events three constraints are applied on jets. They are kinematics cuts on integrated jets, cuts on the b-jets, and cuts on aggregate di-jets. Now a lower limit is selected that four Jets must be detected in final states with cuts on  $p_T$  and  $\eta$  due to uncertainties that come from the efficiency of b-tagging.

These cuts are given in equation (21)

$$p_T^{Jets} \geq 20 \text{ GeV}, |\eta^{Jets}| \leq 3 \quad (21)$$

$\rho_T$  distributions of b-jets for different masses of charged Higgs are shown in **Figure 8**  $P_T$  distributions of  $b(\bar{b})$  quarks of THDM-III. Fig. (a) shows transverse momentum distributions for BP-I and Fig. (b) shows transverse momentum distributions for BP-II figure.caption.28(a-b) and Figure 9  $P_T$  distributions of  $b(\bar{b})$  quarks of THDM-IV. Here, the Fig.9(a) shows transverse momentum distributions for BP-I and Fig.9(b) shows transverse momentum distributions for BP-II figure.caption.29(a-b).

## IX. PSEUDORAPIDITY

Pseudorapidity is an important kinematical variable, and it defines the angle of particle w.r.t beam axis, and it is given by

$$\eta = -\ln \left[ \tan\left(\frac{\theta}{2}\right) \right] \quad (22)$$

Here  $\theta$  is the angle formed by the direction of the beam axis and the three momentum of the particle it is given as;

$$\theta = 2 \tan^{-1}(e^{-\eta}) \quad (23)$$

In terms of the particle's three momenta, the  $\eta$  can be expressed as

$$\eta = \frac{1}{2} \ln \left( \frac{|p| + p_z}{|p| - p_z} \right) \quad (24)$$

From equation(24) we can write as;

$$e^\eta = \sqrt{\frac{|p| + p_z}{|p| - p_z}} \quad (25)$$

&

$$e^{-\eta} = \sqrt{\frac{|p| - p_z}{|p| + p_z}} \quad (26)$$

From the addition of the above two equations we obtain

$$|p| = p_T \cosh \eta$$

where  $p_T$  is transverse momentum and is given as

$$p_T = \sqrt{p^2 - p_z^2}$$

More extensive detail can be found in text [24]. Now in the center of the mass frame, we obtain the peak of distribution at  $y \approx \eta \approx 0$ . **Figure 10**  $\eta$  distributions of  $b(\bar{b})$  quarks of THDM-III. **Fig.a** shows pseudorapidity distribution curves of  $b(\bar{b})$  quarks for BP-I. **Fig. b** shows pseudorapidity distributions of  $b(\bar{b})$  quarks for BP-II **figure.caption.31(a)** and **Figure 10**  $\eta$  distributions of  $b(\bar{b})$  quarks of THDM-III. **Fig.a** shows pseudorapidity distribution curves of  $b(\bar{b})$  quarks for BP-I. **Fig. b** shows pseudorapidity distributions of  $b(\bar{b})$  quarks for BP-II **figure.caption.31(b)** display the  $b(\bar{b})$  quark pseudorapidity distributions for THDM-I and THDM-II models. In **Figure 10(a)** the distribution curves are shown for BP-I of THDM-I and



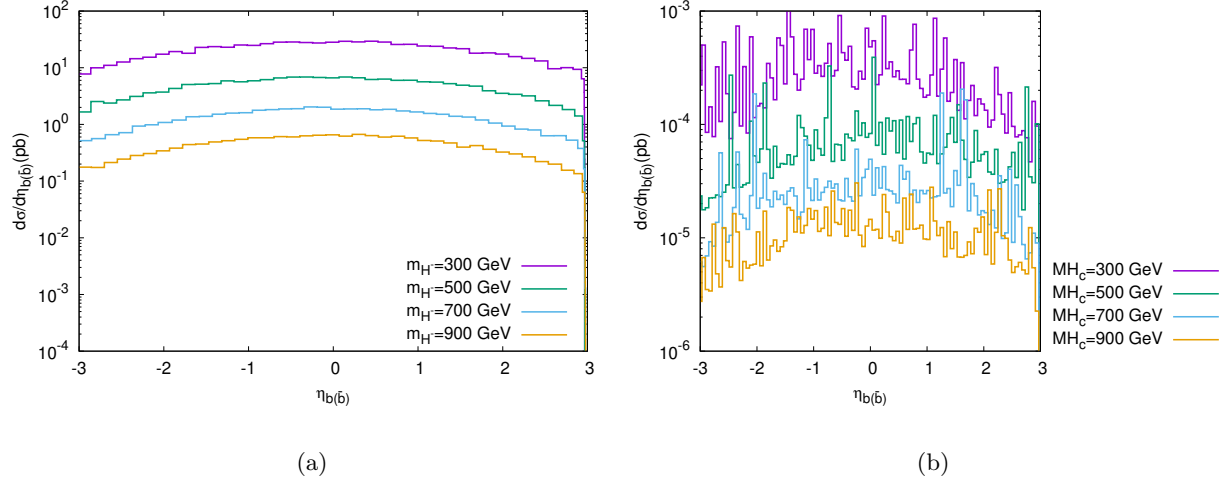


FIG. 10:  $\eta$  distributions of  $b(\bar{b})$  quarks of THDM-III. Fig.a shows pseudorapidity distribution curves of  $b(\bar{b})$  quarks for BP-I. Fig. b shows pseudorapidity distributions of  $b(\bar{b})$  quarks for BP-II

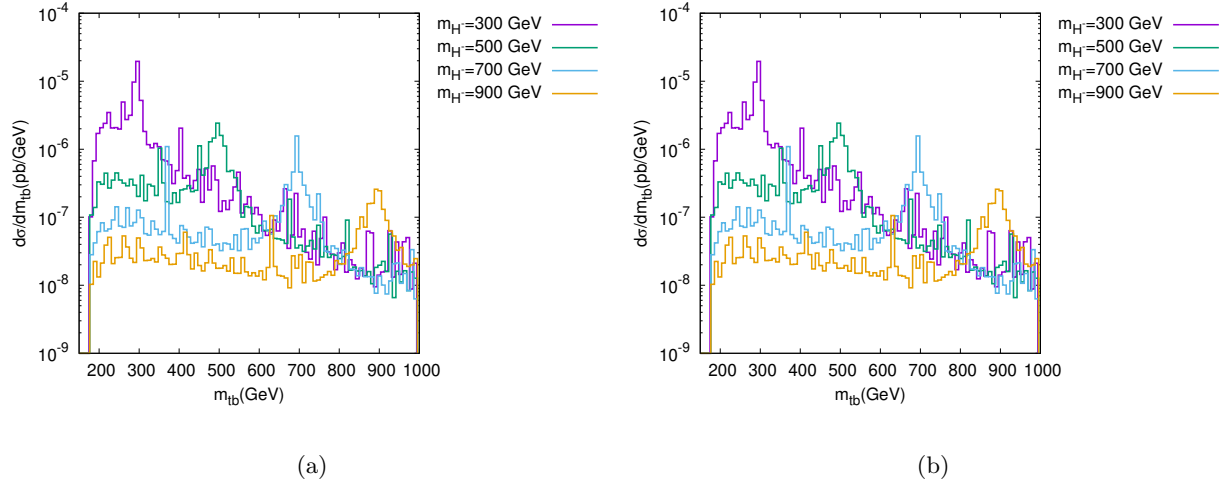


FIG. 11:  $\eta$  distributions of  $b(\bar{b})$  quarks of THDM-IV. Fig a. shows pseudorapidity distribution curves of  $b(\bar{b})$  quarks for BP-I. Fig. b shows Pseudorapidity distributions of  $b(\bar{b})$  quarks for BP-II

in (b) the distributions are given for BP-II of model THDM-I.

In Figure 10(b) the pseudorapidity distributions are plotted for BP-I and in (b) the distributions are plotted for BP-II of model THDM-II.

The distribution decreases when we go towards higher masses, which shows that massive particles are less deflected than lighter particles. Also when peaks are obtained when  $\eta \approx 0$ .

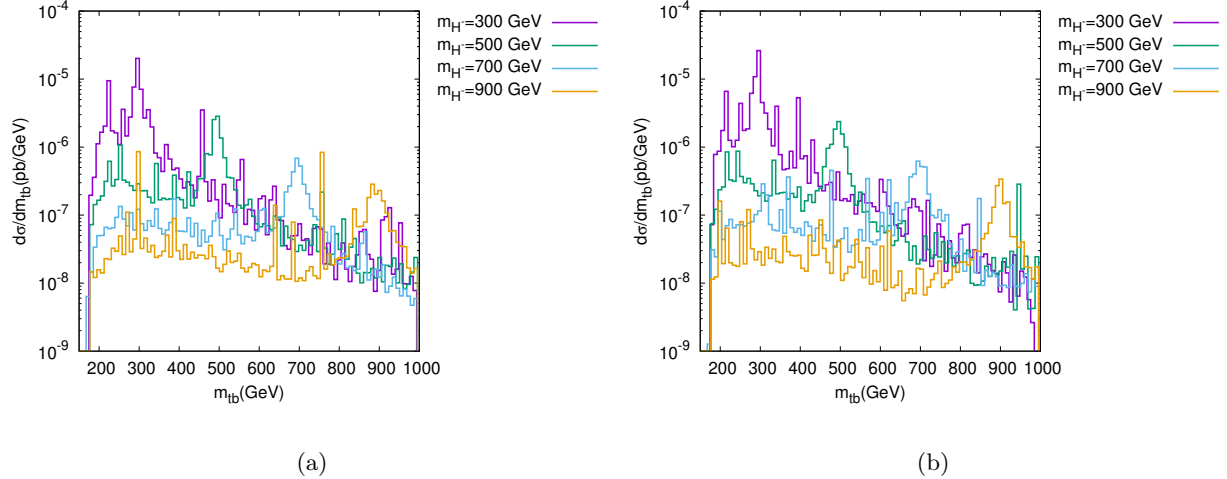


FIG. 12: A view of the THDM-III invariant mass distributions of  $t\bar{b}$  quarks. Fig.a shows  $m_{tb}$  data plots of  $t\bar{b}$  quarks for BP-I. Fig.b shows  $m_{tb}$  of  $t\bar{b}$  quarks for BP-II

## X. INVARIANT MASS

Figure 12A view of the THDM-III invariant mass distributions of  $t\bar{b}$  quarks. Fig.a shows  $m_{tb}$  data plots of  $t\bar{b}$  quarks for BP-I. Fig.b shows  $m_{tb}$  of  $t\bar{b}$  quarks for BP-IIfigure.caption.34 and Figure 13Invariant Mass distributions of  $tb$  quarks of THDM-IV. Fig.a shows  $m_{tb}$  data plots of  $t\bar{b}$  quarks for BP-I. Fig.b shows  $m_{tb}$  of  $t\bar{b}$  quarks for BP-IIfigure.caption.35 show the invariant mass curves of  $t\bar{b}$  quarks for different masses of charged Higgs for both THDM-III and THDM-IV models. One could expect a sharp peak for the distribution of  $\frac{dN}{dm_o}$  at the mass of the missing particle which was not detected during a direct collision.

As scaled earlier there will be a distinct peak at the mass of the missing particle. The sharp peaks can be seen at different Higgs masses. We also have plotted the distributions for SM, which shows no sharp peak indicating the charged Higgs presence behind the SM like two Higgs doublet models, for which phenomenology is discussed in the current studies. One of the important peaks can be seen in Figure 11 $\eta$  distributions of  $b(\bar{b})$  quarks of THDM-IV. Fig a. shows pseudorapidity distribution curves of  $b(\bar{b})$  quarks for BP-I. Fig. b shows Pseudorapidity distributions of  $b(\bar{b})$  quarks for BP-IIfigure.caption.32 of THDM-IV for BP-II. The more sharp peaks are at the Higgs masses  $M_{H^-} = 300$  GeV &  $M_{H^-} = 900$  GeV. For  $M_{H^-} = 500$  GeV &  $M_{H^-} = 700$  GeV the peaks are broader which indicates the error in measurements and is more difficult to detect experimentally. In Figure 11 $\eta$  distributions of  $b(\bar{b})$  quarks of THDM-IV. Fig a. shows pseudorapidity distribution curves of  $b(\bar{b})$  quarks for BP-I. Fig. b shows Pseudorapidity distributions of  $b(\bar{b})$  quarks for BP-

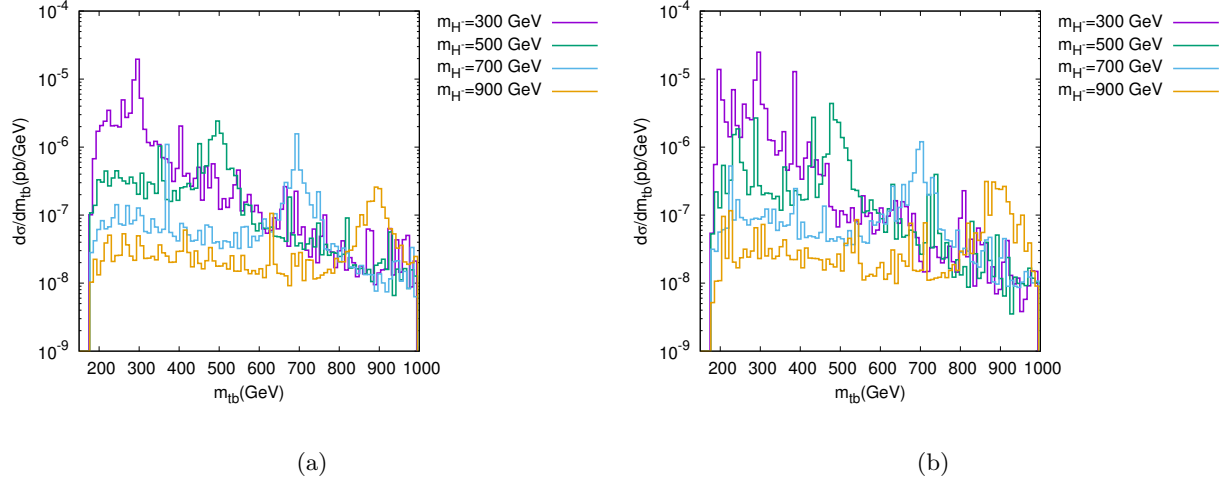


FIG. 13: Invariant Mass distributions of  $t\bar{b}$  quarks of THDM-IV. Fig.a shows  $m_{t\bar{b}}$  data plots of  $t\bar{b}$  quarks for BP-I. Fig.b shows  $m_{t\bar{b}}$  of  $t\bar{b}$  quarks for BP-II

If figure.captio.32(a) for BP-I, the more sharp peak is at  $M_{H^-} = 300\text{GeV}$ . All the rest are broader peaks as compared to charged Higgs of mass 300 GeV.

## XI. OBSERVABILITY OF CHARGED HIGGS USING MULTIVARIATE ANALYSIS

The Multivariate Analysis (MVA) methods have been widely used in many analyses within ATLAS and CMS to discriminate signals over backgrounds in searches that have complex multi-particle final states, e.g. the current analysis of  $pp \rightarrow H^\pm W^\mp \rightarrow t\bar{b}W^\mp \rightarrow b\bar{b}W^\mp W^\pm \rightarrow 2 \text{ bjets} + 2l + \text{MET}$  as signal channel and electroweak processes are considered as background events generating almost similar final states. Based on machine learning, the Multivariate classification technique becomes basic for many of the data analysis methods. It is incorporated with the ROOT framework, the TMVA toolkit has a huge diversity of classification algorithms. Training, testing, progress assessment, and use of all accessible classifiers are executed at the same time and are simple to use. Supervised Machine Learning is used in all TMVA methods. They utilize the training events which determine the required outputs. When implementing a machine learning algorithm to an analysis, a process of training is required that is the algorithm looks at already known events (i.e. simulated samples where right or wrong is predefined) and learns the difference between background and signal events.

We select three different classifiers for the charged Higgs analysis in association with W boson Boosted Decision Trees (BDT), maximum Likelihood (LH) method, and Multilayer Perceptron

(MLP). The production samples are based on Monte Carlo (MC) simulations of the signal as scaled and mostly backgrounds produced at  $\sqrt{s} = 100$  TeV. The main background consists of producing single top quarks in association with W boson, single top production in the s-channel process, top anti-top quark pair production, and their purely leptonic decays.

In Type I 2HDM, the gauge bosons and fermions acquire mass from a single Higgs doublet, while the other Higgs doublet contributes to mass via mixing. The Higgs doublet  $\phi_2$  couples with all quarks (up-type and down-type) and charged leptons, naturally conserving flavor. This is one of two discrete scenarios that achieve natural flavor conservation in 2HDM. The model under consideration requires the calculation of various parameters in the physical basis, including  $m_{12}^2$ ,  $\tan \beta$ , physical Higgs masses ( $m_{H^\pm}, m_A, m_h, m_H$ ), mixing angle  $\alpha$ ,  $\sin(\beta - \alpha)$ ,  $\lambda_6$ , and  $\lambda_7$ .

In this, we operate close to the alignment limiting, where  $\sin(\beta - \alpha) = 0.997806$ . This constraint is equivalent to assuming that the lighter CP-even Higgs boson (h) behaves like the Standard Model Higgs boson. The mass of the lighter Higgs boson is set to the mass of the SM Higgs boson, specifically 125.1 GeV, whereas the heavy neutral Higgs mass is  $m_H = 308.86$  GeV, pseudoscalar Higgs boson mass is  $m_A = 411.99$  GeV and charged Higgs  $m_{H^\pm}$  is set equal to 272.13 GeV. By fixing these parameters and operating at  $\sqrt{s}=100$  TeV with  $\tan\beta=3.66$ , we can simplify the calculation and analysis of the model's properties. Both signal and background processes are produced with Pythia8 [26] embedded in MadGraph [27] and Delphes [28] performs the detector simulation.

We take  $m_h = 125.1$  GeV and randomly scan the remaining 2HDM parameters within the ranges:  $126 \leq m_H \leq 500$  GeV,  $60 \leq m_A \leq 500$  GeV,  $80 \leq m_{H^\pm} \leq 400$  GeV,  $2 \leq \tan\beta \leq 20$ ,  $0.95 \leq \sin(\beta - \alpha) \leq 1$  and  $m_{12}^2 = m_H^2 \sin\beta \cos\beta \text{ GeV}^2$ . All parameter points are required to satisfy the theoretical and experimental constraints. The 2HMDC [29] applies the theoretical constraints e.g., perturbativity, unitarity, and vacuum stability while Electroweak precision constraints through oblique parameters S, T, and U. Similarly, Flavor constraints using SuperIso v4.1 [30] and Exclusion limits at 95% confidence level from BSM Higgs searches at collider experiments using the new version of HiggsBounds [31] via HiggsTools [32].

Both the signal and background samples are analyzed with the Toolkit for Multivariate Analysis toolkit for ROOT [33] with various multivariate classification algorithms. Events are selected as the presence of the required number of objects in the final state. In signal events including at least 2 bjets, where there are at least two leptons and missing transverse energy less than 120 GeV, transverse momentum of leptons greater than 20 GeV and absolute pseudo-rapidity less than 2.1, selection cuts are applied for background suppression and signal enhancement. The Receiver operating characteristic (ROC) curve is a useful tool for evaluating the performance of a classifier

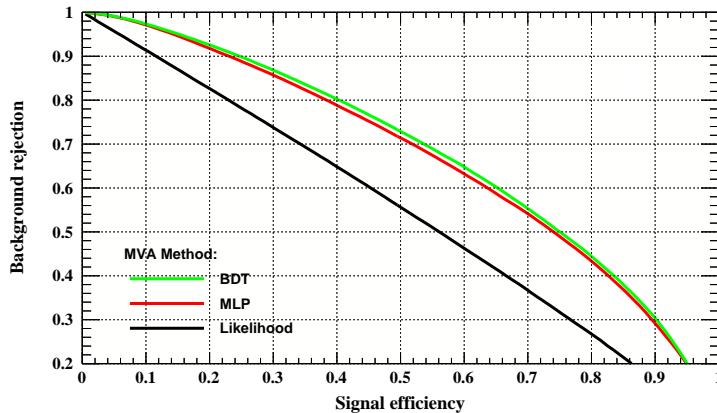


FIG. 14: A view of the signal efficiency and background rejection curve.

MVA Classifier	Optimal-Cut	$\frac{S}{\sqrt{S+B}}$	Sig-Eff	Bkg-Eff
MLP	0.292	160.41	0.972	0.865
Likelihood	-0.272	158.37	0.990	0.964
BDT	-0.140	160.36	0.967	0.849

TABLE I: The Optimal-Cuts, Signal-Background ratio, signal, and Background efficiency for the number of signal and background with applying Cuts.

because it provides a visual representation of the trade-off between sensitivity and specificity. By examining the curve, one can determine the optimal threshold for classification, which is the point at which the model is most effective at distinguishing between positive and negative classes. The response of all three classifiers are shown in Figure 14A view of the signal efficiency and background rejection curve.figure.caption.37 and its values for Area Under the Curve (AUC) are extracted which are MLP=0.67, BDT=0.70, Likelihood=0.6 which demonstrates moderate and satisfactory values except for the Likelihood method. It can be further improved in the future.

We also calculate statistical significance (SS) from the signal (S) and background (B) events, where significance is defined as  $SS = S/\sqrt{S+B}$  as obtained in Table IThe Optimal-Cuts, Signal-Background ratio, signal, and Background efficiency for the number of signal and background with applying Cuts.table.caption.38 which allows the observability of the charged Higgs at FCC designed integrated luminosity. However, statistics must be considered, which means that the

signal efficiency that corresponds to the ideal cut value must be considered. A lot of signals get filtered away if this number is really low. If the real data has low statistics, the cut quality cannot be guaranteed because the output distribution differs from that of the training sample. Figure 16The MLP cut efficiencies as a function of applied cut values.figure.caption.40 shows the MLP cut efficiencies as a function of applied cut value. It has been observed that MLP and BDT have higher significance as compared to the Likelihood method and both are almost equal to each other. Figure 15Signal efficiency, background efficiency, signal purity, signal efficiency multiplied with purity and significance  $S/\sqrt{S+B}$  as a function of BDT cut level in (a) and Likelihood output level in (b) as a function of the BDT cut value.figure.caption.39 shows the significance  $S/\sqrt{S+B}$  as a function of the BDT cut value in (a) and Likelihood cut in (b) for a certain number of signal and background events. This is the measure that most accurately captures the effectiveness of the instruction. A method's performance is assessed using the significance output, where a larger significance denotes a better classifier. Nevertheless, statistical considerations need to be taken into account regarding the signal efficiency that equates to the optimal cut value. If this value is really low, a lot of signal is filtered out. Since the output distribution is different from the training sample's, the quality of the cut cannot be guaranteed if the real data has poor statistics. The MLP cut efficiency as a function of applied cut value is displayed in Figure 16The MLP cut efficiencies as a function of applied cut values.figure.caption.40. It has been noted that MLP and BDT are almost equivalent to each other and are efficient and have more relevance when compared to the Likelihood approach.

## XII. CONCLUSION

A comprehensive analysis has been conducted to predict the observability of charged Higgs across a broad range of parameter space in the extended Higgs sector in the context of extremely high energy proton-proton collisions. The production and decay properties of charged Higgs rely on the ongoing searches of LHC. We have concentrated on the 2HDM model type III & IV scenario, studied the charged Higgs boson, and top quark associated production in proton-proton collisions at the FCC energy.

The Multivariate Analysis methods have been widely used in ATLAS and CMS to discriminate signals over backgrounds in searches with complex multi-particle final states. The TMVA toolkit, which is incorporated with the ROOT framework, offers a variety of classification algorithms. For the charged Higgs analysis in association with a W boson, three different classifiers were selected

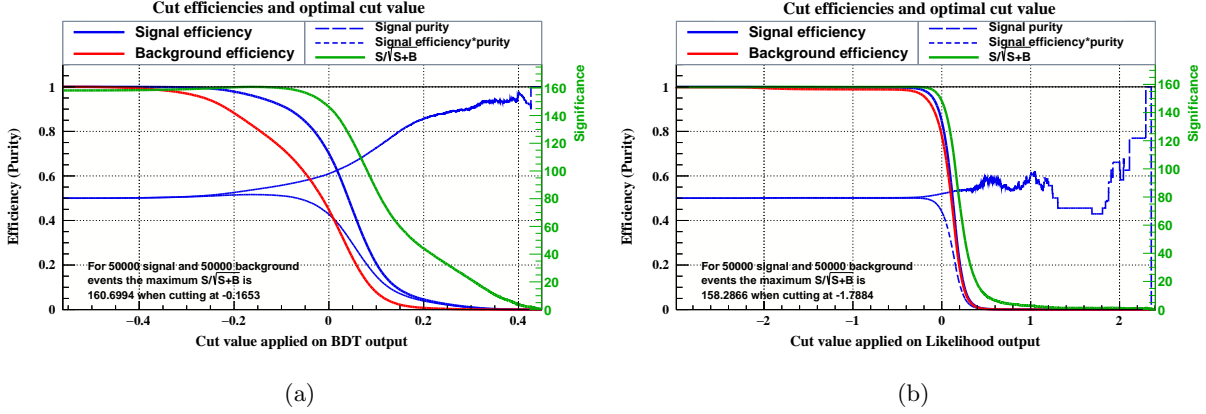


FIG. 15: Signal efficiency, background efficiency, signal purity, signal efficiency multiplied with purity and significance  $S/\sqrt{S+B}$  as a function of BDT cut level in (a) and Likelihood output level in (b) as a function of the BDT cut value.

m

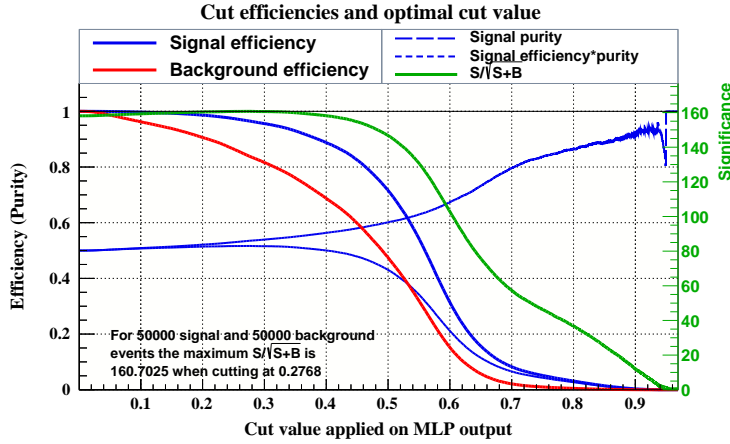


FIG. 16: The MLP cut efficiencies as a function of applied cut values.

e.g., BDT, LH, and MLP. The production samples were based on Monte Carlo simulations of the signal and mostly backgrounds produced at  $\sqrt{s} = 100$  TeV. The main background consists of single top quark production, single top production in the s-channel process, top anti-top quark pair production, and their purely leptonic decays. The model under consideration is a Type I 2HDM, where the gauge bosons and fermions acquire mass from a single Higgs doublet, while the other Higgs doublet contributes to mass via mixing. The parameters of the model were scanned within certain ranges, and the signal and background samples were analyzed using the TMVA toolkit. The Receiver operating characteristic (ROC) curve was used to evaluate the performance of the classifiers, and the results showed that the MLP and BDT methods performed better than the

LH method. The statistical significance (SS) was also calculated from the signal and background events, and it was observed that MLP and BDT had higher significance than LH.

- 
- [1] Aad, G., et al, Observation of a new particle in the search for the Standard Model Higgs boson with the ATLAS detector at the LHC, Phys. Lett. B716, C29 (2012). arXiv:1207.7214[hep-ex]
  - [2] Chatrchyan, S., et al, Observation of a new boson at a mass of 125 GeV with the CMS experiment at the LHC, Phys. Lett. B716, 361 (2012). arXiv:1207.7235[hep-ex]
  - [3] Steven D. Bass, Albert De Roeck, and Marumi Kado, The Higgs boson implications and prospects for future discoveries, Nature 3, 608 (2021).
  - [4] A. G. Akeroyd et al, Prospects for charged Higgs searches at the LHC, Eur. Phys. J. C (2017) 77:276
  - [5] G. C. Branc et al, Theory and Phenomenology of two-Higgs-doublet models, Physics Reports 516 (2012) 1102
  - [6] ALEPH, DELPHI, L3, OPAL, LEP collaboration, G. Abbiendi et al., Search for Charged Higgs bosons: Combined Results Using LEP Data, Eur. Phys. J. C73, 2463 (2013). arXiv:1301.6065
  - [7] I. T. Cakir et al, Probing charged Higgs boson couplings at a future circular hadron collider, Phys. Rev. D 94, 015024 (2016)
  - [8] Shuailong Li, Huayang Song and Shufang Su, Probing exotic charged Higgs decays in the Type-II 2HDM through top rich signal at a future 100 TeV pp collider, JHEP 11, 105 (2020).
  - [9] Vernon Barger, Heather E. Logan, and Gabe Shaughnessy, Identifying extended Higgs models at the LHC, Phys. Rev. D 79, 115018 (2009)
  - [10] Ijaz Ahmed, Sehrish Gul, Taimoor Khurshid Received, Correlation Between the Scaling Factor of the Yukawa Coupling and Cross Section for the  $e^+e^- \rightarrow hhff_{bar}(f \neq t)$  in Type-II 2HDM, Int J Theor Phys 60, 2916-2929 (2021).
  - [11] A. Arhrib et al, Extended Higgs sector of 2HDM with real singlet facing LHC data, Eur. Phys. J. C (2020) 80:13.
  - [12] Rodolfo A. Diaz, R. Martinez, and J.-Alexis Rodriguez, Lepton flavor violation in the two Higgs doublet model type III, Phys. Rev. D, VOLUME 63, 095007 (2001).
  - [13] A. Arhrib et al, Two-Higgs-doublet type-II and -III models and  $t \rightarrow ch$  at the LHC, Eur. Phys. J. C (2016) 76:328.
  - [14] R. Primulando, J. Julio and P. Uttayarat, Collider constraints on lepton flavor violation in the 2HDM, Phys. Rev. D 101, 055021 (2020)
  - [15] Xuewen Liua, Ligong Bianb, Xue-Qian Lia, Jing Shuc, Type-III two Higgs doublet model



- plus a pseudoscalar confronted with  $h \rightarrow \mu\tau$  and dark matter, Nuclear Physics B 909(2016) 507-524
- [16] Heavy Flavor Averaging Group (HFAG) collaboration, Y. Amhis et al., Averages of  $b$ -hadron,  $c$ -hadron, and  $\tau$ -lepton properties as of summer (2014). arXiv:1412.7515
- [17] ATLAS collaboration, G. Aad et al., Search for charged Higgs bosons decaying via  $H^\pm \rightarrow \tau^\pm\nu$  fully hadronic final states using pp collision data at  $\sqrt{s}=8$  TeV with the ATLAS detector, JHEP 03, 088 (2015). arXiv:1412.6663
- [18] CMS collaboration, V. Khachatryan et al., Search for a charged Higgs boson in pp collisions at  $\sqrt{s}=8$  TeV JHEP 11, 018 (2015). arXiv:1508.07774
- [19] CMS collaboration, V. Khachatryan et al., Search for a charged Higgs boson in pp collisions at  $\sqrt{s}=8$  TeV JHEP 11, 018 (2015). arXiv:1508.07774
- [20] ATLAS collaboration, G. Aad et al., Search for charged Higgs bosons decaying via  $H^\pm \rightarrow \tau^\pm\nu$  fully hadronic final states using pp collision data at  $\sqrt{s}=8$  TeV with the ATLAS detector, JHEP 03, 088 (2015). arXiv:1412.6663
- [21] Prasenjit Sanyal, 'Limits on the charged Higgs parameters in the two Higgs doublet model using CMS  $\sqrt{s}=13$  TeV results', The European Physical Journal C volume 79, Article number: 913 (2019).
- [22] M. Guchait and A. H. Vijay, "Probing Heavy Charged Higgs Boson at the LHC," Phys. Rev., Vol. D98, No. 11, p. 115028, 2018.
- [23] David J. Griffiths, Introduction to elementary particles. John Wiley & Sons, Inc, 1987.
- [24] Cheuk-Yin Wong, "Introduction to High-Energy Heavy-Ion Collisions", World Scientific Publishing Co. Pte. Ltd
- [25] A. Hocker, P. Speckmayer, J. Stelzer, J. Therhaag, E. von Toerne, H. Voss, M. Backes, T. Carli, O. Cohen and A. Christov, et al. arXiv:physics/0703039.
- [26] T Sjöstrand, Torbjorn, Stefan Ask, Jesper R. Christiansen, Richard Corke, Nishita Desai, Philip Ilten, Stephen Mrenna, Stefan Prestel, Christine O. Rasmussen, and Peter Z. Skands. "An introduction to PYTHIA 8.2." Computer Physics Communications 191 (2015): 159-177.
- [27] J. Alwall, M. Herquet, F. Maltoni, O. Mattelaer, and T. Stelzer, "MadGraph 5: going beyond", JHEP 06, 128 (2011), arXiv:1106.0522, (2011).
- [28] . de Favereau, C. Delaere, P. Demin, A. Giammanco, V. Lemaître, A. Mertens, and M. Selvaggi. DELPHES 3, A modular framework for fast simulation of a generic collider experiment. JHEP, 02:057, 2014
- [29] D. Eriksson, J. Rathsman and O. Stal, 2HDMC - Two-Higgs-Doublet Model Calculator., Comput. Phys. Commun. 181 (2010) 189.
- [30] F. Mahmoudi, SuperIso v2.3: A program for calculating flavor physics observables in supersymmetry, Computer Physics Communications, Volume 180, Issue 9, 2009, Pages 1579-1613,
- [31] P. Bechtle et al., Comput.Phys.Commun.181:138-167,2010

- [32] P. Bechtle et al., *Comput. Phys. Commun.* 182 (2011), 2605-2631
- [33] Rene Brun and Fons Rademakers, ROOT - An Object Oriented Data Analysis Framework, Proceedings AIHENP'96 Workshop, Lausanne, Sep. 1996, *Nucl. Inst. Meth. in Phys. Res. A* 389 (1997) 81-86.